Lithium Ferrocyanide Catholyte for High-Capacity Aqueous Redox Flow Batteries

Xiaotong Li [†, a], Yuan Yao [†, a], Xin Jia [b], Chenxi Liu [a], Jiahuang Jian [a], Bao Guo [a], Kai Cui [a], Songtao Lu [a], Yang Li [a], Wei Qin[*,b], Qing Wang[*,c] and Xiaohong Wu[*,a]

Mrs. X. Li, Prof. Y. Yao, Miss. C. Liu, Mr. J. Jian, Mr. B. Guo, Mr. K. Cui, Prof. S. Lu, Prof. Y. Li, and Prof. X. Wu
School of Chemistry and Chemical Engineering, Harbin Institute of Technology, Harbin 150001, China
E-mail: **wuxiaohong@hit.edu.cn (X.W.)**

Mr. X. Jia and Prof. W. Qin
School of Materials Science and Engineering, Harbin Institute of Technology, Harbin 150001, China
E-mail: **qinwei@hit.edu.cn (W.Q.)**

Prof. Q. Wang
Department of Materials Science and Engineering, National University of Singapore, 117576, Singapore
E-mail: **msewq@nus.edu.sg (Q.W.)**

† These authors contributed equally to this work.

Abstract

The design of electrolyte materials with both tunable redox potential and high solubility is critical for boosting the energy density of aqueous redox flow batteries (ARFBs) for stationary energy storage. A redox-active material lithium ferrocyanide ($Li_4[Fe(CN)_6]$) is designed. $Li_4[Fe(CN)_6]$ has an improved solubility of 2.3 M compared to other ferrocyanide salts due to week intermolecular interactions. The constructed $Li_4[Fe(CN)_6]$-based ARFB system demonstrates high average capacity retention (nearly 100%) over 1365 hours and an unprecedented volumetric capacities up to 62.2 Ah/L in H_2O. A zinc-ferricyanide ($Zn/[Fe(CN)_6]^{3-}$) ARFB, using a Nafion 117 membrane, achieves an unprecedented catholyte capacity of 61.4 Ah/L at neutral pH, surpassing the performance of most known ARFBs. In addition, the prepared ARFB shows a low electrolyte cost of $24 per kWh. This work provides a promising option for developing sustainable energy storage technology with high efficiency and a low cost.

Keywords: aqueous redox flow battery, energy storage, intermolecular interaction, redox-active material, $Li_4[Fe(CN)_6]$, solubility.

Toc-graphics

The designed redox-active material, **lithium ferrocyanide ($Li_4[Fe(CN)_6]$)**, exhibits the solubility of 2.32 M, much higher than $Na_4[Fe(CN)_6]$ (0.56 M) and $K_4[Fe(CN)_6]$ (0.76 M). It endows the constructed lithium ferrocyanide-based half ARFB system with high volumetric capacities up to 62.2 Ah/L in H_2O, which is the highest value in all reported aqueous electrolytes.

1. Introduction

Aqueous redox flow batteries (ARFBs) have been regarded as a promising technology for stationary energy storage owing to their unique design of decoupled energy and power[1-7]. However, their low energy density, determined by the redox potential and solubility of redox-active materials (RAMs), is the main obstacle for achieving high energy storage[8-14]. The solubility of RAMs depends mainly on the solute's intermolecular and intramolecular interactions with the solvent in the RFBs[15, 16]. Solutes with weak intramolecular interactions generally correspond to high solubility in water[17-19]. At present, many methods have been proposed to increase the concentration of RAMs[20], such as molecular engineering[21-23], constructing eutectic systems[24-26], physical modification(add additives)[24, 27], and redox targeting strategies[28-30], etc. By judiciously tuning the intermolecular interactions, molecular engineering is a promising strategy to increase the solubility of RAMs[15, 31-33]. Molecular engineering has significantly improved the solubility of various RAMs[15, 34, 35], such as alloxazine[36], viologen[21], ferrocene[22], and TEMPO[37].

The dissolution of a RAM is dictated by the change in the Gibbs free energy (ΔG_s^Θ) when it is mixed with a solvent, which is further determined by the enthalpy change (ΔH_s^Θ) and the entropy change (ΔS_s^Θ)[38]. ΔH_s^Θ consists of the changes in the interactions between molecules[26], while ΔS_s^Θ is the change in the randomness of the system[39, 40]. In thermodynamics, ΔS_s^Θ is mostly positive due to the increase in the molecular degrees of freedom when the solvent and solute are miscible[41, 42]. In general, the intermolecular interactions between different components have a significant impact on the solubility of RAMs, and the intermolecular interactions between different components depends on the paired anions or cations.

Ferrocyanide salts, such as sodium ferrocyanide ($Na_4[Fe(CN)_6]$) and potassium ferrocyanide ($K_4[Fe(CN)_6]$), have been used as RAMs for RFBs. Na^+ has a much stronger polarization with $[Fe(CN)_6]^{4-}$ than K^+, thereby increasing the covalent bond component between Na^+ and $[Fe(CN)_6]^{4-}$. Thus, the anions and cations in $Na_4[Fe(CN)_6]$ are relatively difficult to dissociate. This is the reason why $Na_4[Fe(CN)_6]$ has a lower solubility than $K_4[Fe(CN)_6]$. To improve the solubility of ferrocyanide salts, the interactions between the ferrocyanide and water molecules should be much stronger than those within the ferrocyanide, making the cation and $[Fe(CN)_6]^{4-}$ much easier to separate. Li^+ has a much smaller radius than Na^+ and K^+, resulting in a substantial polarization effect with water molecules, rendering it easily separable from $[Fe(CN)_6]^{4-}$. Thus, it is predicted that the $Li_4[Fe(CN)_6]$ compound might have a higher solubility than $Na_4[Fe(CN)_6]$ and $K_4[Fe(CN)_6]$.

Motivated by this, we synthesized $Li_3[Fe(CN)_6]$) and $Li_4[Fe(CN)_6]$ to prove the above hypothesis. $Li_4[Fe(CN)_6]$ exhibits a significantly improved solubility of 2.32 M, which is much higher than those of $Na_4[Fe(CN)_6]$ and $K_4[Fe(CN)_6]$. As a RAM, $Li_4[Fe(CN)_6]$ provides a high average capacity retention (nearly 100%) over 1365 hours and a charge capacities up to 62.2 Ah/L in H_2O, which is the highest value thus far in the literature. The corresponding neutral $Zn/[Fe(CN)_6]^{3-}$ flow battery with a Nafion 117 membrane has achieved an energy density of 75.5 Wh/L. Its coulombic and energy efficiencies are 99.91% and 83.91% at 40 mA/cm^2, respectively. The capacity retention rate per cycle is 99.9934% for over 540 h. Benefiting from the low cost of $Li_4[Fe(CN)_6]$, the RFBs also show a considerable advantage economically for their practical application in the future.

2. Results and Discussion

2.1. Prepare of $Li_3[Fe(CN)_6]$ and $Li_4[Fe(CN)_6]$

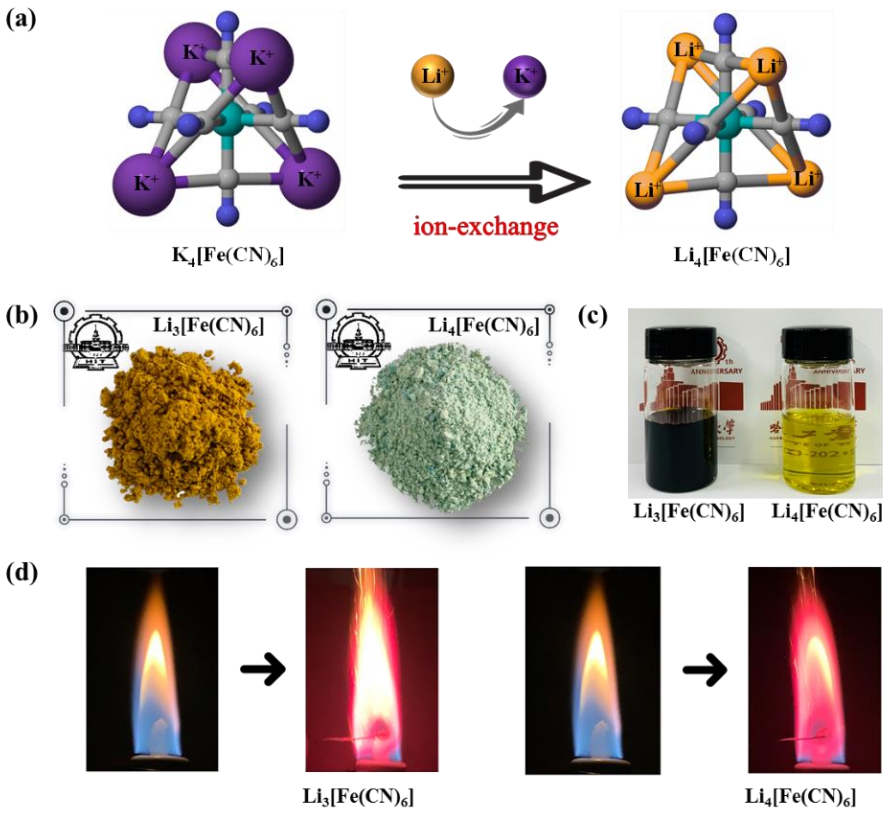

Figure 1. (**a**) Scheme of the cation-exchange reactions to prepare $Li_3[Fe(CN)_6]$ and $Li_4[Fe(CN)_6]$, and (**b**) photographs of the products. (**c**) $Li_3[Fe(CN)_6]$ and $Li_4[Fe(CN)_6]$ aqueous solutions and (**d**) their flame reactions.

$Li_3[Fe(CN)_6]$ and $Li_4[Fe(CN)_6]$ were prepared from $K_3[Fe(CN)_6]$ and $K_4[Fe(CN)_6]$, respectively, through a cation-exchange strategy with nearly 100% yield rate (Figure 1a and Supplementary Figure S1). After vacuum freeze-drying treatment to remove water, orange $Li_3[Fe(CN)_6]$ powder and light green $Li_4[Fe(CN)_6]$ powder were obtained (Figure 1b), which reveal dark and light yellow color in solution (Figure 1c), respectively. The completion of the cation exchange was evaluated by flame reaction, showing the predominant presence of Li element (Figure 1d). The elemental analysis further confirmed the absence of crystal water in the products (Supplementary Table S1). The solubility of all the materials was measured using the ultraviolet-

visible (UV-Vis) spectroscopy (Supplementary Figure S3). The solubility of $Li_4[Fe(CN)_6]$ was calculated to be 2.32 M, much higher than those of $Na_4[Fe(CN)_6]$ (0.56 M) and $K_4[Fe(CN)_6]$ (0.76 M). The corresponding volume capacity of $Li_4[Fe(CN)_6]$ was estimated to be as high as 62.2 Ah/L, while those of $Na_4[Fe(CN)_6]$ and $K_4[Fe(CN)_6]$ were 15.0 and 20.4 Ah/L, respectively.

To explain that $Li_4[Fe(CN)_6]$ shows much higher solubility than other ferrocyanide salts, the key factors affecting the solubility of ionic compounds were scrutinized. Normally, they mainly include (1) external conditions such as the temperature, (2) intramolecular interactions of the solute (i.e., van der Waals forces, ion polarization, etc.), and (3) intermolecular interactions between the solute and solvent (i.e., ion polarization, hydrogen bonds, etc.). At constant temperature and pressure, these interactions would play a decisive role in determining the solubility of ionic compounds. We first considered $Na_4[Fe(CN)_6]$ and $K_4[Fe(CN)_6]$, for which the intermolecular interactions of the solute are mainly contributed by ion polarization. The mutual polarization of anions and cations can increase the covalent bond component in the ionic bond. The stronger the polarization is, the larger the covalent bond component is. Na^+ has a smaller radius of 102 pm than K^+ (138 pm), resulting in that the former has much stronger polarization with $[Fe(CN)_6]^{4-}$ and much larger covalent bond component. Therefore, this explains the fact that the solubility of $Na_4[Fe(CN)_6]$ in water is lower than that of $K_4[Fe(CN)_6]$. Thermodynamically, the solubility can be assessed based on the free energy changes (ΔG_s^Θ) of the substance in the process of dissolving in water according to the following formula:

$$\Delta G_s^\Theta = \Delta H_s^\Theta - T\Delta S_s^\Theta \qquad \text{(Equation 1)}$$

Generally, the enthalpy change (ΔH_s^Θ) in the dissolution process has a dominant effect on the solubility of the substance, while the entropy change (ΔS_s^Θ) also plays an important role for salts composed of single-charge. Large-radius IA group alkali metal cations (except lithium), due

to the fact that they exhibit a large positive entropy change in water (Supplementary Table S2), i.e., 59 and 102.5 J/K·mol for $S_s^{\Theta}(Na^+)$ and $S_s^{\Theta}(K^+)$, respectively. Therefore, the entropy change term cannot be ignored. For K^+, because of its larger radius, ΔG_s^{Θ} of the dissolution process is determined by ΔS_s^{Θ}. In comparison, Na^+ has a smaller radius and a bigger lattice energy for $Na_4[Fe(CN)_6]$, therefore, both the $\Delta H_s^{\Theta}$and ΔS_s^{Θ} determine the ΔG_s^{Θ} of the dissolution process of $Na_4[Fe(CN)_6]$. As a result, $\Delta G_s^{\Theta}(K_4[Fe(CN)_6])$ is more negative than $\Delta G_s^{\Theta}(Na_4[Fe(CN)_6])$, which renders that $K_4[Fe(CN)_6]$ is more soluble than $Na_4[Fe(CN)_6]$.

If the interactions between the solute molecule and the solvent molecule are stronger than those within the respective molecules, it would facilitate the separation of anion and cation of the solute molecule. Li^+ has the smallest radius of 76 pm in the IA group[43], resulting in significantly different chemical properties from other alkali cations when forming ionic compounds. The difference in the radii of Li^+ and $[Fe(CN)_6]^{4-}$ is the largest, resulting in that the anions ($[Fe(CN)_6]^{4-}$) and cations (Li^+) would not be in close contact in ionic crystals and Li^+ could produce a stronger polarization effect on water molecules. Upon mixing with water, due to their strong polarization, water molecules can easily squeeze through and surround Li^+ (Supplementary Figure S4), reducing the attraction between Li^+ and $[Fe(CN)_6]^{4-}$ and thus enhancing its solubility. From the perspective of thermodynamics, although Li^+ has the smallest radius, the compound has the largest lattice energy. Since Li^+ has a stronger hydration effect than other alkali metals, the increase in enthalpy of hydration is more significant than the increase in lattice energy. This is also reflected by the standard molar formation enthalpy of ions in an aqueous solution ($\Delta_f H_m^{\Theta}$) (Supplementary Figure S5 and Supplementary Table S3). In comparison, the entropy term of Li^+ is so small which could be ignored. Therefore, for the Li compound, the enthalpy term plays a decisive role in ΔG_s^{Θ} of the dissolution process. With the above, $Li_4[Fe(CN)_6]$ compound presents a more negative ΔG_s^{Θ} than

$Na_4[Fe(CN)_6]$ and $K_4[Fe(CN)_6]$ and consequently a higher solubility. Ferricyanide salts of different cations (Li^+, Na^+ and K^+) have the similar tendency to dissolve and are not discussed here.

The dissolution enthalpies (ΔH_s^Θ) of the six substances were measured in water under ambient conditions. As listed in Supplementary Table S4, the ΔH_s^Θ ($Li_4[Fe(CN)_6]$) in water is more negative than those of $K_4[Fe(CN)_6]$ and $Na_4[Fe(CN)_6]$, showing that $Li_4[Fe(CN)_6]$ releases more heat when dissolved in water, according to Equation 2. This contribution is mainly due to the stronger hydration of Li^+.

$$\Delta H_s^\Theta(M'_4Fe(CN)_6,s)=4\Delta H_s^\Theta(M'^+,aq)+\Delta H_s^\Theta(Fe(CN)_6^{4-},aq)-\Delta_f H_m^\Theta(M'_4Fe(CN)_6,s) \quad \text{(Equation 2)}$$

As shown in Supplementary Table S4, the standard molar formation enthalpy $\Delta_f H_m^\Theta$ of $Li_4[Fe(CN)_6]$ is greater than that of $K_4[Fe(CN)_6]$ and $Na_4[Fe(CN)_6]$. This is due to the smaller radius of Li^+ contributing to the larger lattice energy. It is also consistent with Density functional theory (DFT) calculations on $Li_4[Fe(CN)_6]$ and $K_4[Fe(CN)_6]$ that the energy required to sequentially dissociate Li^+ is greater than that for K^+ (Supplementary Table S5). The dissolution process of an ionic compound is the change from a crystal state to hydrated ions, in which crystal dissociation and ion hydration are involved. Therefore, the interactions between cations and water molecules were calculated. Supplementary Table S6 shows that the ΔG of hydrated Li^+ is much more negative than that of K^+ due to its stronger polarization with water, making the competitive water-solute molecule interaction stronger than the solute molecule interaction. This strong interaction releases considerable heat to offset the heat absorbed by breaking the lattice energy, resulting in the lowest ΔH_s^Θ. This is also consistent with the measured ΔH_s^Θ.

2.2. Physicochemical Properties of $[Fe(CN)_6]^{4-/3-}$-based Catholytes

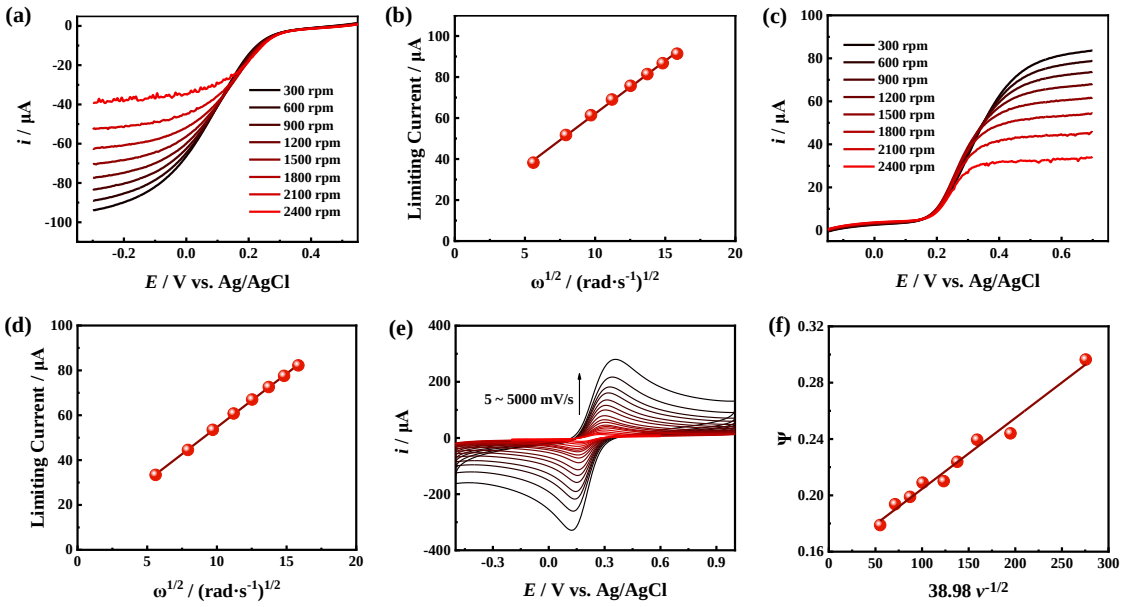

Figure 2. (**a**) RDE LSV curves of 1.0 mM $Li_3[Fe(CN)_6]$ in 0.5 M LiCl solution at a variable rotational speed. (**b**) Plot of i vs. $\omega^{1/2}$. (**c**) RDE LSV curves of 1.0 mM $Li_4[Fe(CN)_6]$ in 0.5 M LiCl solution at a variable rotational speed. (**d**) Plot of i vs. $\omega^{1/2}$. (**e**) CV curves of 2.0 mM $Li_3[Fe(CN)_6]$ and 2.0 mM $Li_4[Fe(CN)_6]$ mixed in a 0.5 M LiCl water solution at variable scan rates and at room temperature. (**f**) Plot of Ψ values vs. $v^{-1/2}$.

The fundamental physicochemical properties of $M'_4[Fe(CN)_6]/M'_3[Fe(CN)_6]$, ($M'=Li^+$, Na^+, K^+, NH_4^+) were investigated, and the results are listed in Table 1. Compared to $Na_4[Fe(CN)_6]$ and $K_4[Fe(CN)_6]$, the aqueous solution of $Li_4[Fe(CN)_6]$ at the same concentration has the lowest conductivity, which is due to relatively small molar conductivity of Li^+. Most electrolytes have low conductivity due to their low solubility. Usually, a certain supporting electrolyte (NaCl, KCl, LiCl, NH_4Cl, etc.) needs to be added to increase the conductivity of the electrolyte. However, due to a high solubility, the ionic conductivity of the saturated $Li_4[Fe(CN)_6]$ solution is higher than those of $Na_4Fe(CN)_6$ (0.56 M, 188 mS/cm) and $K_4Fe(CN)_6$ (0.76 M, 233 mS/cm). For example, saturated $Li_3[Fe(CN)_6]$ and $Li_4[Fe(CN)_6]$ solutions have an ionic conductivity of 349 and 313

mS/cm at room temperature, respectively. They have high conductivity as electrolytes, and no need to add any supporting electrolyte, which reduces the electrolyte cost of ARFBs.

Next, electrochemical studies were carried out to examine how the cation species affect the electrochemical behavior of active materials. The cyclic voltammetry studies revealed that these ferrocyanide compounds have almost identical redox potentials (Supplementary Figure S6 and Supplementary Table S7). To further understand how the different cations affect the dynamics of the active materials, the diffusion coefficients (D) of $[Fe(CN)_6]^{3-}$ and $[Fe(CN)_6]^{4-}$ in 0.5 M M'Cl (M'=Li^+, Na^+, K^+, and NH_4^+) solutions were measured by linear sweep voltammetry (LSV) using a glassy carbon rotating disk working electrode (Figure 2a-d and Supplementary Figures S7-9a-d). As shown in Table 1, one can see that the diffusion coefficients of $[Fe(CN)_6]^{3-}$ and $[Fe(CN)_6]^{4-}$ show very small differences with different cations. The diffusion coefficients *D* of $[Fe(CN)_6]^{3-}$ and $[Fe(CN)_6]^{4-}$ are calculated to be 5.69×10^{-6} and 5.38×10^{-6} cm^2/s in 0.5 M LiCl solution, respectively.

Table 1. Solubility, capacity, electrochemical kinetics data of various alkali metal ferricyanide and ferrocyanide compounds in aqueous solution at room temperature.

Compound (In water)	Solubility (M)	Capacity (Ah/L)		D(cm^2/s)	D_0(cm^2/s)	K^0(cm/s)
$Li_3[Fe(CN)_6]$	2.70	72.4	In 0.5 M LiCl	5.69×10^{-6}	5.38×10^{-6}	1.50×10^{-1}
$Li_4[Fe(CN)_6]$	2.32	62.2		5.07×10^{-6}		
$Na_3[Fe(CN)_6]$	1.20	32.2	In 0.5 M NaCl	5.38×10^{-6}	5.15×10^{-6}	2.73×10^{-2}
$Na_4[Fe(CN)_6]$	0.56	15.0		4.93×10^{-6}		
$K_3[Fe(CN)_6]$	1.31	35.1	In 0.5 M KCl	6.01×10^{-6}	5.95×10^{-6}	5.75×10^{-2}
$K_4[Fe(CN)_6]$	0.76	20.4		5.89×10^{-6}		
$(NH_4)_3[Fe(CN)_6]$	1.92	51.5	In 0.5 M NH_4Cl	6.38×10^{-6}	5.33×10^{-6}	1.70×10^{-1}
$(NH_4)_4[Fe(CN)_6]$	1.60	42.9		4.29×10^{-6}		

Following Nicholson's method[44, 45], solutions containing 2.0 mM $M'_4[Fe(CN)_6]$ (M'=Li^+, Na^+, K^+, NH_4^+) and 2.0 mM $M'_3[Fe(CN)_6]$ in 0.5 M M'Cl were used to obtain cyclic voltammetry

(CV) data at different scan rates, in order to obtain the heterogeneous standard electron transfer rate constant k^0 (Figure 2e and f and Supplementary Figures S7-9e and f). The detailed calculations are included in the Supplementary Information. As summarized in Table 1, $Li_4[Fe(CN)_6]$ and $Li_3[Fe(CN)_6]$ have faster electron transfer rates than their sodium, potassium, and ammonium counterparts. These enhanced electron transfer rates would be beneficial to the energy efficiency and power performance of a RFB. The high solubilities, high conductivities, high volumetric capacities, fast diffusion coefficients, and large heterogeneous standard electron transfer rate constants of $Li_4[Fe(CN)_6]$ and $Li_3[Fe(CN)_6]$ demonstrate that they are great promising redox-active materials for application in ARFBs.

2.3. Half-Cell ARFB Studies with a $Li_4[Fe(CN)_6]$ Catholyte

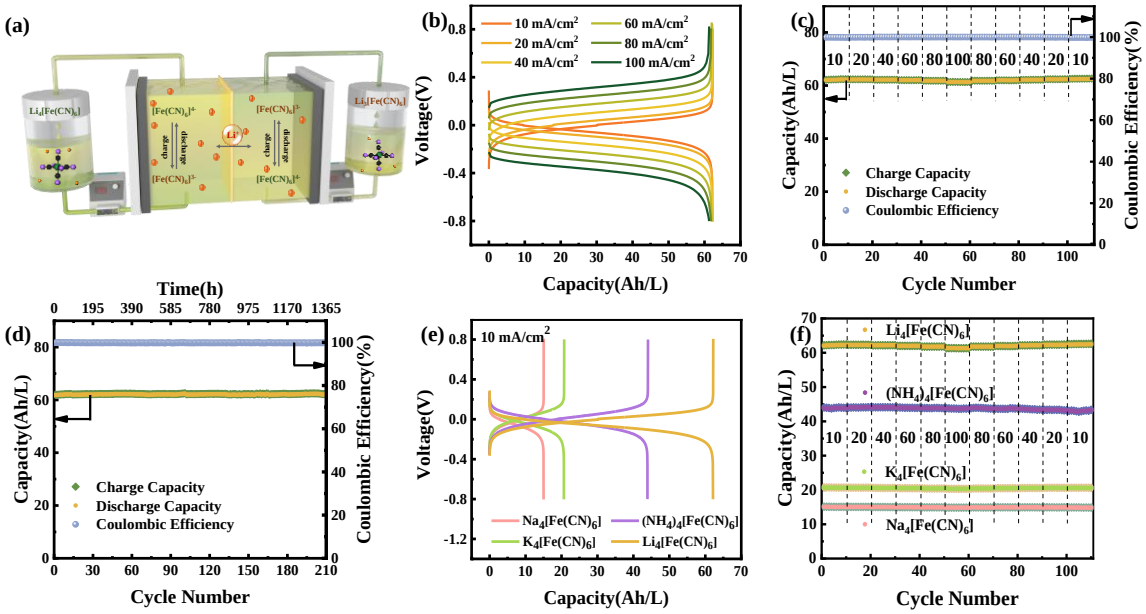

Figure 3. (**a**) Scheme of the $Li_4[Fe(CN)_6]/Li_3[Fe(CN)_6]$ half-cell RFB. (**b**) Representative charge and discharge profiles of the 2.32 M $Li_4[Fe(CN)_6]/Li_3[Fe(CN)_6]$ battery at different current densities. (**c**) Current rate performance of the 2.32 M $Li_4[Fe(CN)_6]/Li_3[Fe(CN)_6]$ battery from 10 to 100 to 10 mA/cm^2. (**d**) Long-term 1365 h testing data of the 2.32 M $Li_4[Fe(CN)_6]/Li_3[Fe(CN)_6]$ half-cell RFB at 10 mA/cm^2: capacity and coulombic efficiency versus time. (**e**) Charge and

discharge curves of the half-cell flow battery containing 0.56 M $Na_4[Fe(CN)_6]/Na_3[Fe(CN)_6]$ (pink), 0.76 M $K_4[Fe(CN)_6]/K_3[Fe(CN)_6]$ (green), 1.60 M $(NH_4)_4[Fe(CN)_6]/(NH_4)_3[Fe(CN)_6]$ (purple), and 2.32 M $Li_4[Fe(CN)_6]/Li_3[Fe(CN)_6]$ (orange) at a current density of 10 mA/cm^2. (**f**) Capacity versus cycling number from 10 to 100 at a current density of 10 mA/cm^2 for the half-cell flow batteries containing 0.56 M $Na_4[Fe(CN)_6]/Na_3[Fe(CN)_6]$, 0.76 M $K_4[Fe(CN)_6]/K_3[Fe(CN)_6]$, 1.60 M $(NH_4)_4[Fe(CN)_6]/(NH_4)_3[Fe(CN)_6]$, and 2.32 M $Li_4[Fe(CN)_6]/Li_3[Fe(CN)_6]$.

The robustness The robustness of a redox-active electrolyte is an important factor that determines the long-term cycling stability of the RFBs. Symmetric flow cell device has been extensively employed in evaluating the cycling stability of redox couples in RFBs[46]. Therefore, to evaluate the chemical stability and reliability of the $Li_4[Fe(CN)_6]/Li_3[Fe(CN)_6]$ redox couple during charge/discharge cycling, a symmetric flow cell (Figure 3a) was assembled with 2.32 M $Li_4[Fe(CN)_6]$ and $Li_3[Fe(CN)_6]$ as the catholyte and anolyte using a Nafion 117 membrane. The electrode areas of the cell were set to 13.5 cm^2 for both the anode and cathode. The rate performance of the battery was measured at currents varied from 10 to 100 and again down to 10 mA/cm^2, and the cutoff voltages were set at 0.8 V for charging and -0.8 V for discharging (Figure 3b). Ten consecutive cycles at each current density achieved a stable capacity retention rate (Figure 3c). Low ohmic loss are observed when the currents varied from 10 to 100 mA/cm^2 attribute to the high conductivity of the electrolytes; moreover, the capacity utilization rate changes only slightly, remaining stable. At every current density, the coulombic efficiency of the cell is close to 100%. Notably, 2.32 M represents the highest concentration and volumetric capacity (62.2 Ah/L) of the $[Fe(CN)_6]^{4-/3-}$-based ARFBs.

Prolonged cycling of the $Li_4[Fe(CN)_6]/Li_3[Fe(CN)_6]$ flow battery was tested at a current density of 10 mA/cm^2 for more than 1365 testing hours (Figure 3d) and 60 mA/cm^2 for 2000 cycles

(Supplementary Figure S10). At a current density of 10 mA/cm^2, the capacity remains unchanged after more than 1365 testing hours. (Supplementary Figure S11), indicating that the $Li_4[Fe(CN)_6]/Li_3[Fe(CN)_6]$ redox-active couple has excellent stability at high concentrations. UV-Vis spectroscopy was performed with the electrolyte after charge and discharge cycling for more than 1365 h to explore the possible chemical degradation of the positive and negative electrolytes. Compared to the original positive and negative electrolytes, the UV-Vis spectrum of the electrolyte after cycling remains unchanged, showing its superb stability (Supplementary Figure S12). CV tests further confirm the electrochemical stability of $Li_4[Fe(CN)_6]$ and $Li_3[Fe(CN)_6]$ in the redox cycle. As shown in Supplementary Figure S13, after long-term charge and discharge cycling of the flow cell, the CV curves of the positive and negative electrolytes overlap well with the original electrolytes. The results prove that $Li_4[Fe(CN)_6]$ and $Li_3[Fe(CN)_6]$ have excellent chemical and electrochemical stability, indicating that $Li_4[Fe(CN)_6]$ and $Li_3[Fe(CN)_6]$ are dependable redox-active materials for ARFB applications.

For comparison, similar flow cell tests were performed using a Nafion 117 membrane and saturated $Na_4[Fe(CN)_6]/Na_3[Fe(CN)_6]$ (0.56 M), $K_4[Fe(CN)_6]/K_3[Fe(CN)_6]$ (0.76 M), and $(NH_4)_4[Fe(CN)_6]/(NH_4)_3[Fe(CN)_6]$ (1.60 M) redox pairs. As shown in Figure 3e and f, the battery capacities of these cell are less than that of the $Li_4[Fe(CN)_6]/Li_3[Fe(CN)_6]$ cell, demonstrating that $Li_4[Fe(CN)_6]$ and $Li_3[Fe(CN)_6]$ are excellent electrolyte materials for ARFB applications.

The resistance of ion-exchange membrane for the conduction of charge balancing ions is critical to the ohmic loss of RFBs upon operation, which significantly affects the energy efficiency and power density of RFBs. Hence, it is imperative to understand the influence of different cations when paired with ferrocyanide on the battery performance. The influence of the cation-exchange membrane (Nafion 117) and an M'Cl (M'=Li^+, Na^+, K^+, and NH_4^+) electrolyte on battery resistance

was first studied through electrochemical impedance spectroscopy (EIS) studies (Supplementary Figure S14 and Supplementary Table S9). The membrane resistance in LiCl is determined to be 1.41 $\Omega \cdot cm^2$, which is lower than that in NaCl (3.18 $\Omega \cdot cm^2$), KCl (3.71 $\Omega \cdot cm^2$), and NH_4Cl (1.94 $\Omega \cdot cm^2$). These results indicate that the Li^+ cation has the highest ion conductivity across the membrane compared to the other four cations, which along with the superior ionic conductivity of the electrolyte solution renders $Li_4[Fe(CN)_6]$-based electrolyte reduced ohmic loss in battery.

2.4. Full ARFB Studies with a $Li_4[Fe(CN)_6]$ Catholyte and Zn Anolyte

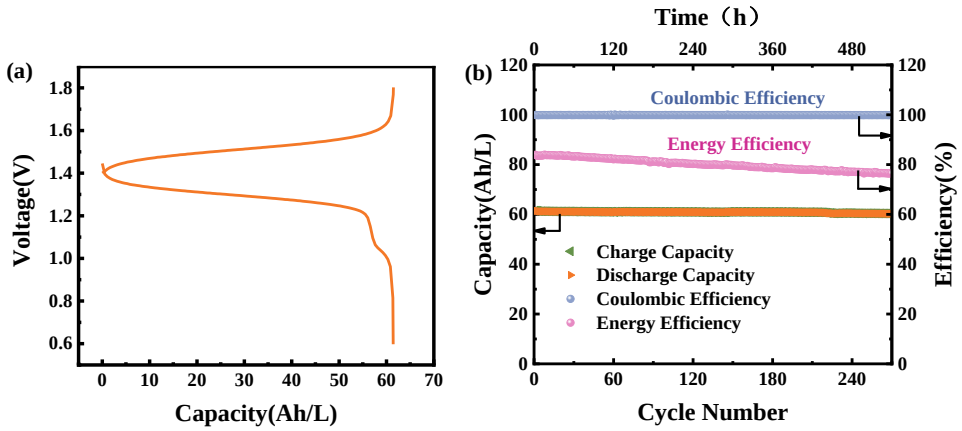

Figure 4. (**a**) Representative charge and discharge curves of the Zn/$[Fe(CN)6]^{3-}$ hybrid flow cell at 40 mA/cm^2. (**b**) Capacity, coulombic, and energy efficiencies of the cell after prolonged cycling. Conditions: anolyte of 70 mL 0.25 M $ZnCl_2$ in 6.4 M LiCl aqueous solution and catholyte of 8.5 mL 2.3 M $Li_3[Fe(CN)_6]$ in water; Nafion 117 cation-exchange membrane; cutoff voltages of 1.8 V for charging and 0.6 V for discharging.

According to the basic research on $[Fe(CN)_6]^{3-}$ and $[Fe(CN)_6]^{4-}$ in various supporting electrolytes at different pH values, it has been determined that $[Fe(CN)_6]^{3-}$ and $[Fe(CN)_6]^{4-}$ have better stability under neutral or near-neutral conditions[47]. A neutral zinc–iron flow battery consisting of a Zn/Zn^{2+} pair that serves as the negative redox couple and the $[Fe(CN)_6]^{3-}$/$[Fe(CN)_6]^{4-}$ pair is employed as the positive redox-active material. Under neutral pH conditions

zinc ions should be in the solvated Zn^{2+} form. The solvated Zn^{2+} will cross the cation exchange membrane, leading to the formation of solid ZnHCF (the zinc form of Prussian blue), which will ultimately lead to capacity loss in the system. To minimize this situation, a relatively low zinc ion concentration is used as the anode. Herein, the $Li_4[Fe(CN)_6]$ electrolyte, with its higher volumetric capacity, is incorporated into the flow battery to increase the energy density. In water, solutions of 0.25 M $ZnCl_2$ in 6.40 M LiCl and 2.30 M $Li_3[Fe(CN)_6]$ were used as the negative and positive electrolytes, respectively. A carbon felt electrode with an active area of 13.5 cm^2 and a Nafion 117 membrane were also employed in the cell. The cell was charged and discharged at a invariable current density of 40 mA/cm^2, resulting in a volumetric discharging capacity of 61.4 Ah/L. The charge and discharge curves are shown in Figure 4a. The battery exhibits an electrolyte utilization of 99.7% at a theoretical catholyte capacity of 61.6 Ah/L and an energy density of 75.5 Wh/L, along with a coulombic efficiency (CE) of 99.91%, energy efficiency (EE) of 83.91%, and voltage efficiency (VE) of 83.99%. The cycling performance was measured at a current density of 40 mA/cm^2 to confirm the reliability and practicality of the zinc–iron flow battery. Overall cycling stability with a capacity retention of nearly 98.2% (99.9934% per cycle or 99.92% per day) was obtained for more than 270 cycles with a CE over 99.86% and an EE of nearly 76.45%. This behavior appears due to the uneven electrostripping/electroplating of Zn on the anodes that always leads to enlarged polarization (energy efficiency fading) or even cell blockage (low cycling stability).

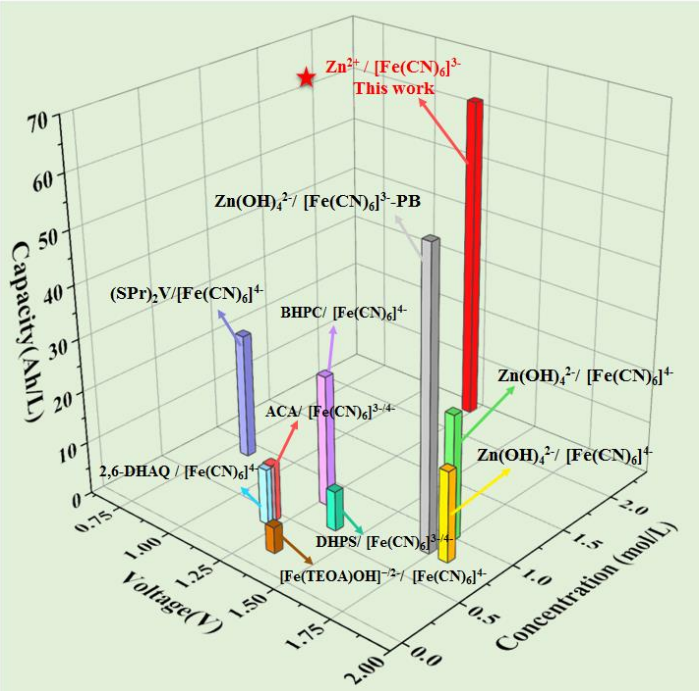

Figure 5. Capacity, concentration of $[Fe(CN)_6]^{4-/3-}$ and cell voltage of the Zn/$[Fe(CN)_6]^{4-/3-}$ RFB and its comparison with other recently reported $[Fe(CN)_6]^{4-/3-}$-based aqueous flow cells. Detailed data are shown in Supplementary Table S10.

In addition to the excellent cycling stability, this battery is economical and has a superior volumetric capacity compared to other reported flow batteries (Figure 5). The energy density delivered by the neutral zinc–iron flow battery is comparable to or significantly higher than that of the best reported aqueous RFBs. Benefiting from the low cost $Li_4[Fe(CN)_6]$ that can be commercialized on an industrial scale, the chemical cost of the pH-neutral zinc–iron flow battery is estimated to be approximately $24 per kWh based on the catholyte (see the detailed cost analysis in the Supplementary Information). In addition, considering the $[Fe(CN)_6]^{3-}$/$[Fe(CN)_6]^{4-}$ redox pair has a fast one-electron redox chemical reaction on an inexpensive carbon felt electrode, even in the absence of a catalyst, the cost incurred to form a battery stack and for system maintenance can be further reduced. These salient characteristics endow the $Li_4[Fe(CN)_6]$/$Li_3[Fe(CN)_6]$ electrolyte

system, and the flow batteries made from them, with a considerable competitive advantages in terms of performance, cost, and safety, showing broad prospects for use in large-scale energy storage.

3. Conclusion

In summary, an interaction-based strategy for designing redox-active molecules with high solubility was proposed to achieve RFBs with a high energy density. The chemical analysis combined with the basic principles of thermodynamics and DFT calculations showed that the solubility of redox-active materials is improved through the intermolecular interactions between the solutes and solvents. Due to the strong polarization between Li^+ and water molecules, a large amount of heat would be released during hydration, offsetting most of the lattice energy. Therefore, the $Li_4[Fe(CN)_6]$ redox-active material designed in this research exhibited 4, 3, and 1.4 times the solubility of $Na_4[Fe(CN)_6]$, $K_4[Fe(CN)_6]$, and $(NH_4)_4[Fe(CN)_6]$, respectively. $Li_4[Fe(CN)_6]$ and $Li_3[Fe(CN)_6]$ exhibited excellent solubility and stability, making them great promising redox-active materials for redox flow battery applications. The demonstrated pH-neutral zinc ferricyanide ($Zn/[Fe(CN)_6]^{3-}$) ARFB had an actual catholyte capacity of 61.4 Ah/L and a CE and EE of 99.91% and 83.91%, respectively, at 40 mA/cm^2, representing the highest volumetric capacity ARFB reported to date. Due to low material costs, a neutral $Zn/[Fe(CN)_6]^{3-}$ ARFB is a promising electrolyte system and the associated flow battery for future commercial energy storage applications. Additionally, it is anticipated that this strategy can be used to design RAMs with broad applicability in flow cells and other electrochemical systems.

4. Experimental Section/Methods

4.1 Chemicals and Materials

All chemicals were purchased from Aladdin Ltd. (Shanghai, China) or Sigma–Aldrich Co. (St. Louis, MO, USA). All chemicals were of analytical purity and utilized directly without further purification. Deionized water (18.2 MΩ cm) was used throughout the experiment.

4.2 UV-Vis Spectroscopy Measurements

The solubility of all materials was calculated based on the UV-Vis spectra of the solutions at different concentrations following the reported method. A METASH Model 8000 spectrometer was used to obtain the UV-Vis spectra of the original electrolyte, anolyte and catholyte after 500 charge/discharge cycles and being diluted.

4.3 Electrochemical Study:

Electrochemical measurements based on linear sweep voltammetry (LSV), cyclic voltammetry (CV), and electrochemical impedance spectroscopy (EIS) studies were performed using a CHI 760E electrochemical workstation. A standard three-electrode system was employed with a glassy carbon electrode as the working electrode, Pt foil as the counter electrode and a Ag/AgCl (3.0 M KCl) electrode as the reference electrode ($E_{RHE} = E_{Ag/AgCl} + 0.208 + 0.059 \times$ pH V; RHE represents the reversible hydrogen electrode.).

4.4 Half-Cell Flow Battery Tests

For the $Li_4[Fe(CN)_6]/Li_3[Fe(CN)_6]$ half-cell flow battery, a cell structure with two carbon felt electrodes (4.5 × 3.0 cm^2) on each side of a Nafion 117 membrane as positive and negative electrodes was prepared, and a silicon gasket and silicon tubing were employed.

4.5 Full-Cell Flow Battery Tests

The setup of the pH-neutral zinc–iron flow cell was the same as that of the $Li_4[Fe(CN)_6]/Li_3[Fe(CN)_6]$ half-cell battery. The cell was galvanostatically charged to 1.8 V and discharged to 0.6 V at a current density of 40 mA/cm^2.

Conflicts of Interest

The authors declare no competing financial interest.

Author Contributions

X.L., Y.Y., X.W., Q.W., and W.Q. conceived the idea. X. L. and Y.Y. designed and performed most of experiments and analyzed the data. Y.Y. carried out the theoretical calculations. C.L. assisted with the material preparation. X.J., J.J., B.G., K.C., S.L., and Y.L. helped to analyze the data and discuss. X.L., Y.Y., X.W., Q.W., and W.Q. wrote the paper. X.W., W.Q. and Q.W. supervised the whole work.

Acknowledgements

This work was supported by the National Natural Science Foundation of China (No. U2067216, U2130109) and Heilongjiang Touyan Team (HITTY-20190033).

Supporting Information

Supplementary material associated with this article can be found, in the online version, at doi:***

References

[1] Feng, R.; Zhang, X.; Murugesan, V.; Hollas, A.; Chen, Y.; Shao, Y.; Walter, E.; Wellala, N. P. N.; Yan, L.; Rosso, K. M.; et al. Reversible ketone hydrogenation and dehydrogenation for aqueous organic redox flow batteries. *Science* **2021**, *372* (6544), 836-840. DOI: doi:10.1126/science.abd9795.

[2] Li, Z.; Lu, Y.-C. Material design of aqueous redox flow batteries: fundamental challenges and mitigation strategies. *Adv. Mater.* **2020**, *32* (47), 2002132. DOI: https://doi.org/10.1002/adma.202002132.

[3] Xu, J.; Pang, S.; Wang, X.; Wang, P.; Ji, Y. Ultrastable aqueous phenazine flow batteries with high capacity operated at elevated temperatures. *Joule* **2021**, *5* (9), 2437-2449. DOI: https://doi.org/10.1016/j.joule.2021.06.019.

[4] Liu, B. L. a. J. Progress and directions in low-cost redox-flow batteries for large-scale energy storage. *Natl. Sci. Rev.* **2017**, *4* (1), 91–105, Review. DOI: 10.1093/nsr/nww098.

[5] Shi, Y.; Wang, Z.; Yao, Y.; Wang, W.; Lu, Y.-C. High-areal-capacity conversion type iron-based hybrid redox flow batteries. *Energy Environ. Sci.* **2021**, 10.1039/D1EE02258J. DOI: 10.1039/D1EE02258J.

[6] Wang, W.; Luo, Q. T.; Li, B.; Wei, X. L.; Li, L. Y.; Yang, Z. G. Recent progress in redox flow battery research and development. *Adv. Funct. Mater.* **2013**, *23* (8), 970 – 986, Article. DOI: 10.1002/adfm.201200694.

[7] Zhao, Y.; Ding, Y.; Song, J.; Peng, L. L.; Goodenough, J. B.; Yu, G. H. A reversible Br_2/Br^- redox couple in the aqueous phase as a high-performance catholyte for alkaliion batteries. *Energy & Environmental Science* **2014**, *7* (6), 1990–1995, Article. DOI: 10.1039/c4ee00407h.

[8] Cameron, J. M.; Holc, C.; Kibler, A. J.; Peake, C. L.; Walsh, D. A.; Newton, G. N.; Johnson, L. R. Molecular redox species for next-generation batteries. *Chem. Soc. Rev.* **2021**, *50* (10), 5863–5883, 10.1039/D0CS01507E. DOI: 10.1039/D0CS01507E.

[9] Narayanan, T. M.; Zhu, Y. G.; Gençer, E.; McKinley, G.; Shao-Horn, Y. Low-cost manganese dioxide semi-solid electrode for flow batteries. *Joule* **2021**. DOI: https://doi.org/10.1016/j.joule.2021.07.010.

[10] Fornari, R. P.; Mesta, M.; Hjelm, J.; Vegge, T.; de Silva, P. Molecular engineering strategies for symmetric aqueous organic redox flow batteries. *ACS Mater. Lett.* **2020**, *2* (3), 239–246. DOI: 10.1021/acsmaterialslett.0c00028.

[11] Luo, J. A.; Hu, B.; Hu, M. W.; Zhao, Y.; Liu, T. L. Status and prospects of organic redox flow batteries toward sustainable energy storage. *ACS Energy Lett.* **2019**, *4* (9), 2220–2240, Review. DOI: 10.1021/acsenergylett.9b01332.

[12] Poizot, P.; Gaubicher, J.; Renault, S.; Dubois, L.; Liang, Y. L.; Yao, Y. Opportunities and challenges for organic electrodes in electrochemical energy storage. *Chem. Rev.* **2020**, *120* (14), 6490–6557, Review. DOI: 10.1021/acs.chemrev.9b00482.

[13] Li, X.; Gao, P.; Lai, Y.-Y.; Bazak, J. D.; Hollas, A.; Lin, H.-Y.; Murugesan, V.; Zhang, S.; Cheng, C.-F.; Tung, W.-Y.; et al. Symmetry-breaking design of an organic iron complex catholyte for a long cyclability aqueous organic redox flow battery. *Nat. Energy* **2021**, *6* (9), 873–881. DOI: 10.1038/s41560-021-00879-6.

[14] Yuan, Z. Z.; Yin, Y. B.; Xie, C. X.; Zhang, H. M.; Yao, Y.; Li, X. F. Advanced materials for zinc-based flow battery: development and challenge. *Adv. Mater.* **2019**, *31* (50), 1902025, Review. DOI: 10.1002/adma.201902025.

[15] Ding, Y.; Zhang, C.; Zhang, L.; Zhou, Y.; Yu, G. Pathways to widespread applications: development of redox flow batteries based on new chemistries. *Chem* **2019**, *5* (8), 1964–1987. DOI: https://doi.org/10.1016/j.chempr.2019.05.010.

[16] Zhang, C.; Niu, Z.; Peng, S.; Ding, Y.; Zhang, L.; Guo, X.; Zhao, Y.; Yu, G. Phenothiazine-based organic catholyte for high-capacity and long-life aqueous redox flow batteries. *Adv. Mater.* **2019**, *31* (24), 1901052. DOI: https://doi.org/10.1002/adma.201901052.

[17] Duan, W.; Huang, J.; Kowalski, J. A.; Shkrob, I. A.; Vijayakumar, M.; Walter, E.; Pan, B.; Yang, Z.; Milshtein, J. D.; Li, B.; et al. "Wine-dark sea" in an organic flow battery: storing negative charge in 2,1,3-benzothiadiazole radicals leads to improved cyclability. *ACS Energy Lett.* **2017**, *2* (5), 1156–1161. DOI: 10.1021/acsenergylett.7b00261.

[18] Shimizu, A.; Takenaka, K.; Handa, N.; Nokami, T.; Itoh, T.; Yoshida, J.-I. Liquid quinones for solvent-free redox flow batteries. *Adv. Mater.* **2017**, *29* (41), 1606592. DOI: https://doi.org/10.1002/adma.201606592.

[19] Wang, G.; Huang, B.; Liu, D.; Zheng, D.; Harris, J.; Xue, J.; Qu, D. Exploring polycyclic aromatic hydrocarbons as an anolyte for nonaqueous redox flow batteries. *J. Mater. Chem. A* **2018**, *6* (27), 13286–13293, 10.1039/C8TA03221A. DOI: 10.1039/C8TA03221A.

[20] Chen, H.; Zhou, Y.; Lu, Y.-C. Lithium–organic nanocomposite suspension for high-energy-density redox flow batteries. *ACS Energy Lett.* **2018**, *3* (8), 1991–1997. DOI: 10.1021/acsenergylett.8b01257.

[21] DeBruler, C.; Hu, B.; Moss, J.; Liu, X.; Luo, J.; Sun, Y.; Liu, T. L. Designer two-electron storage viologen anolyte materials for neutral aqueous organic redox flow batteries. *Chem* **2017**, *3* (6), 961–978. DOI: https://doi.org/10.1016/j.chempr.2017.11.001.

[22] Hu, B.; DeBruler, C.; Rhodes, Z.; Liu, T. L. Long-cycling aqueous organic redox flow battery (AORFB) toward sustainable and safe energy storage. *J. Am. Chem. Soc.* **2017**, *139* (3), 1207–1214. DOI: 10.1021/jacs.6b10984.

[23] Robertson, L. A.; Li, Z.; Cao, Y.; Shkrob, I. A.; Tyagi, M.; Smith, K. C.; Zhang, L.; Moore, J. S.; Z, Y. Observation of microheterogeneity in highly concentrated nonaqueous electrolyte solutions. *J. Am. Chem. Soc.* **2019**, *141* (20), 8041–8046. DOI: 10.1021/jacs.9b02323.

[24] Zhang, C.; Niu, Z.; Ding, Y.; Zhang, L.; Zhou, Y.; Guo, X.; Zhang, X.; Zhao, Y.; Yu, G. Highly Concentrated Phthalimide-Based Anolytes for Organic Redox Flow Batteries with Enhanced Reversibility. *Chem* **2018**, *4* (12), 2814-2825. DOI: https://doi.org/10.1016/j.chempr.2018.08.024.

[25] Zhang, C.; Zhang, L.; Ding, Y.; Guo, X.; Yu, G. Eutectic electrolytes for high-energy-density redox flow batteries. *ACS Energy Lett.* **2018**, *3* (12), 2875–2883. DOI: 10.1021/acsenergylett.8b01899.

[26] Zhang, C.; Zhang, L.; Yu, G. Eutectic electrolytes as a promising platform for next-generation electrochemical energy storage. *Acc. Chem. Res.* **2020**, *53* (8), 1648–1659. DOI: 10.1021/acs.accounts.0c00360.

[27] Yuan, Z.; Liu, X.; Xu, W.; Duan, Y.; Zhang, H.; Li, X. Negatively charged nanoporous membrane for a dendrite-free alkaline zinc-based flow battery with long cycle life. *Nat. Commun.* **2018**, *9* (1), 3731. DOI: 10.1038/s41467-018-06209-x.

[28] Chen, Y.; Zhou, M. Y.; Xia, Y. H.; Wang, X.; Liu, Y.; Yao, Y.; Zhang, H.; Li, Y.; Lu, S. T.; Qin, W.; et al. A Stable and High-Capacity Redox Targeting-Based Electrolyte for Aqueous Flow Batteries. *Joule* **2019**, *3* (9), 2255-2267. DOI: 10.1016/j.joule.2019.06.007.

[29] Yan, R.; Wang, Q. Redox-Targeting-Based Flow Batteries for Large-Scale Energy Storage. *Adv. Mater.* **2018**, *30* (47), 1802406. DOI: https://doi.org/10.1002/adma.201802406.

[30] Yu, J. Z.; Wang, X.; Zhou, M. Y.; Wang, Q. A redox targeting-based material recycling strategy for spent lithium ion batteries. *Energy Environ. Sci.* **2019**, *12* (9), 2672-2677. DOI: 10.1039/c9ee01478k.

[31] Kwabi, D. G. Molecular engineering expands the chemical possibilities for organic flow batteries. *Joule* **2021**, *5* (7), 1636-1638. DOI: https://doi.org/10.1016/j.joule.2021.06.023.

[32] Luo, J.; Hu, B.; Hu, M.; Zhao, Y.; Liu, T. L. Status and prospects of organic redox flow batteries toward sustainable energy storage. *ACS Energy Lett.* **2019**, *4* (9), 2220–2240. DOI: 10.1021/acsenergylett.9b01332.

[33] Zhang, C.; Zhang, L.; Ding, Y.; Peng, S.; Guo, X.; Zhao, Y.; He, G.; Yu, G. Progress and prospects of next-generation redox flow batteries. *Energy Storage Mater.* **2018**, *15*, 324–350. DOI: https://doi.org/10.1016/j.ensm.2018.06.008.

[34] Zhang, L.; Zhao, B.; Zhang, C.; Yu, G. Insights into the redox chemistry of organosulfides towards stable molecule design in nonaqueous energy storage systems. *Angew. Chem. Int. Ed.* **2021**, *60* (8), 4322–4328. DOI: https://doi.org/10.1002/anie.202013264.

[35] Zu, X.; Zhang, L.; Qian, Y.; Zhang, C.; Yu, G. Molecular engineering of azobenzene-based anolytes towards high-capacity aqueous redox flow batteries. *Angew. Chem. Int. Ed.* **2020**, *59* (49), 22163–22170. DOI: https://doi.org/10.1002/anie.202009279.

[36] Lin, K.; Gómez-Bombarelli, R.; Beh, E. S.; Tong, L.; Chen, Q.; Valle, A.; Aspuru-Guzik, A.; Aziz, M. J.; Gordon, R. G. A redox-flow battery with an alloxazine-based organic electrolyte. *Nat. Energy* **2016**, *1* (9), 16102, Article. DOI: 10.1038/nenergy.2016.102 Scopus.

[37] Janoschka, T.; Martin, N.; Hager, M. D.; Schubert, U. S. An aqueous redox-flow battery with high capacity and power: the TEMPTMA/MV system. *Angew. Chem. Int. Ed.* **2016**, *55* (46), 14427–14430. DOI: https://doi.org/10.1002/anie.201606472.

[38] Alkhatib, I. I. I.; Bahamon, D.; Llovell, F.; Abu-Zahra, M. R. M.; Vega, L. F. Perspectives and guidelines on thermodynamic modelling of deep eutectic solvents. *J. Mol. Liq.* **2020**, *298*, 112183. DOI: https://doi.org/10.1016/j.molliq.2019.112183.

[39] Alhadid, A.; Mokrushina, L.; Minceva, M. Design of Deep Eutectic Systems: A Simple Approach for Preselecting Eutectic Mixture Constituents. *Molecules* **2020**, *25* (5), 1077.

[40] Kollau, L. J. B. M.; Vis, M.; van den Bruinhorst, A.; Tuinier, R.; de With, G. Entropy models for the description of the solid–liquid regime of deep eutectic solutions. *J. Mol. Liq.* **2020**, *302*, 112155. DOI: https://doi.org/10.1016/j.molliq.2019.112155.

[41] Sun, H.; Li, Y.; Wu, X.; Li, G. Theoretical study on the structures and properties of mixtures of urea and choline chloride. *J. Mol. Model.* **2013**, *19* (6), 2433–2441. DOI: 10.1007/s00894-013-1791-2.

[42] Baclig, A. C.; McConohy, G.; Poletayev, A.; Michelson, A.; Kong, N.; Lee, J.-H.; Chueh, W. C.; Rugolo, J. High-Voltage, Room-Temperature Liquid Metal Flow Battery Enabled by Na-K|K-β″-Alumina Stability. *Joule* **2018**, *2* (7), 1287-1296. DOI: https://doi.org/10.1016/j.joule.2018.04.008.

[43] Li, Y.; Lu, Y.; Adelhelm, P.; Titirici, M.-M.; Hu, Y.-S. Intercalation chemistry of graphite: alkali metal ions and beyond. *Chemical Society Reviews* **2019**, *48* (17), 4655-4687, 10.1039/C9CS00162J. DOI: 10.1039/C9CS00162J.

[44] Lavagnini, I.; Antiochia, R.; Magno, F. An Extended Method for the Practical Evaluation of the Standard Rate Constant from Cyclic Voltammetric Data. *Electroanalysis* **2004**, *16* (6), 505-506. DOI: 10.1002/elan.200302851.

[45] Nicholson, R. S. Theory and Application of Cyclic Voltammetry for Measurement of Electrode Reaction Kinetics. *Analytical Chemistry* **2002**, *37* (11), 1351-1355. DOI: 10.1021/ac60230a016.

[46] Leung, P.; Shah, A. A.; Sanz, L.; Flox, C.; Morante, J. R.; Xu, Q.; Mohamed, M. R.; Ponce de León, C.; Walsh, F. C. Recent developments in organic redox flow batteries: A critical review. *Journal of Power Sources* **2017**, *360*, 243-283. DOI: https://doi.org/10.1016/j.jpowsour.2017.05.057.

[47] DeBruler, C.; Hu, B.; Moss, J.; Liu, X.; Luo, J.; Sun, Y.; Liu, T. L. Designer Two-Electron Storage Viologen Anolyte Materials for Neutral Aqueous Organic Redox Flow Batteries. *Chem* **2017**, *3* (6), 961-978. DOI: https://doi.org/10.1016/j.chempr.2017.11.001.